Constraints on Mars' recent equatorial wind regimes from light-toned layered deposits and comparison with general circulation model results

E. Sefton-Nash[a], N. A. Teanby[b], C. Newman[c], R. A. Clancy[b], M. I. Richardson[c]

[a]*Department of Earth and Space Sciences, University of California Los Angeles, 595 Charles Young Drive East, Los Angeles, CA 90095, USA*
[b]*School of Earth Sciences, University of Bristol, Queen's Road, BS8 1RJ, UK*
[c]*Ashima Research, 600 S. Lake Ave., Suite 104, Pasadena, CA 91106, USA.*

Abstract

Aeolian modification has been the dominant surface process on Mars throughout the Amazonian. Orientations of aeolian features such as dunes and yardangs are controlled by the prevailing wind regime during the feature's formation. Therefore, observation of recently formed bedform orientations provides a way to probe Mars' recent wind regime and constrain/test general circulation models (GCMs). We collect statistical distributions of transverse dune and yardang azimuths at nine sites on Mars, and compare measured feature orientations to those predicted by using vector wind field output from the MarsWRF GCM. We focus on interior layered deposits because their young surface age (0.1-10Ma) and erodible nature makes them applicable to determination of Mars' modern wind regime. Our methods of mapping from the long-term wind field to predicted feature orientations include consideration of wind stress thresholds for sand movement to occur, sand flux equations, and the direction of maximum gross bedform-normal transport. We find that all methods examined typically agree with each other to within $\sim$15°, though there are some exceptions using high order wind stress weightings with multi-directional annual wind fields. Generally, use of higher wind stress thresholds produces improved matches to dune orientations.

Comparison of multiple yardang orientations to annually variable wind fields is accomplished by inspection of directional maxima in modeled wind vector frequency distributions. Yardangs match well to model predictions

and sub-populations in close proximity to each other are shown to match individual directional maxima in GCM output for a single site, implying that topographic effects may produce very localized unidirectional wind fields unresolved by the GCM.

Keywords: Mars, aeolian, GCM, palaeoclimate, dunes, yardangs, GBNT

---

1. Introduction

Aeolian features on Mars' surface are transient on a range of timescales. Relatively short-lived features such as wind streaks and active dunes are representative of present day surface wind regimes, while less transient features such as yardangs, ventifacts and fretting are a product of the time-integrated, changing wind regimes over longer timescales. In this study we compare orientation distributions of dunes and yardangs to examine agreement between their inferred formative wind fields.

Aeolian feature orientations may be used to validate the capability of global circulation models (GCMs) to predict surface wind fields. Previous comparisons of aeolian feature orientations with those predicted from Mars GCMs (Haberle et al., 1993; Greeley et al., 1993; Gardin et al., 2012) have shown that there is often not agreement between modelled wind vectors and those inferred from the orientations of aeolian features, at least when rather straightforward mappings are assumed (e.g., when yardang orientations are compared to the seasonally-averaged wind directions predicted by a GCM). Climate forcing by the combination of orbital eccentricity cycles and precession of Mars' spin axis (Ward, 1979b) has been shown by Fenton and Richardson (2001) not to cause sufficient change to surface wind fields to account for the observed disagreement, for obliquity $<45°$, though more significant changes to the surface wind field have been noted for obliquities exceeding 45° (Newman et al., 2005).

It has also been suggested that changes to local topography, climate or polar wander may also have occurred (Fenton and Richardson, 2001).

However, several other factors may also contribute to the disparity, including (but not limited to): (i) low GCM resolution compared to local topographic variation (meaning that the model cannot properly capture the feature-forming wind field); (ii) uncertainty regarding the physical properties of the surface that are key to aeolian processes (such as sediment availability, grain size distributions, and fine-scale surface roughness), or (iii) choice of

numerical mapping between GCM surface wind vectors and predicted feature orientation (which is impeded by gaps in our understanding of sediment transport, dune formation, and rock erosion, both for Mars and in general). We explore in particular the impact of (iii) in this work.

While surface wind dynamics and erosion rates on Mars differ greatly from those on Earth, relationships developed through field observation, laboratory experiments, and modeling form the basis for much of our understanding of aeolian processes on Mars (e.g. Bagnold (1941); Greeley et al. (1982); Bitter (1963a,b); Merrison et al. (2008); Rubin and Hunter (1987)). While some aspects of Mars' erosional environment are well-constrained, others are largely unknown (see (ii) and (iii) above). In an attempt to better understand the remaining disparities between predicted and observed aeolian features, we test a range of numerical mappings between wind vectors output by the MarsWRF GCM (Richardson et al., 2007; Toigo et al., 2012) and predicted bedform orientations (see (iii) above). These are described in detail in Section 3.2; here we merely note that the formation mechanisms for dunes (depositional features) and yardangs (erosional features) are very different, and thus we cannot use the same mapping to predict the orientations of both sets of features. As an example, while we would expect a unidirectional wind field to produce transverse linear dunes (or Barchan where sand supply is limited) with crests oriented normal to the wind direction, we would expect the same wind field to produce yardangs oriented parallel to the wind direction - i.e., at 90° to the dunes. This is because the dunes are built from scratch via the accumulation of sand, while the yardangs are produced by the removal of rock material from around the sides of an existing feature as the wind is deflected around it. For more complex wind regimes, however, theory suggests that dunes will form with an orientation that maximizes gross bedform-normal transport (GBNT) of surface material (Rubin and Hunter, 1987) (see Sections 2.2 and 3.2), while yardang orientations may perhaps be more controlled by the dominant wind direction (see Section 2.3). Thus a 90° offset between dune and yardang orientations need not generally occur. We compare our predictions to the observed populations of dunes and yardangs at nine sites (Figures 1 and 2) selected for their highly wind-eroded nature. Sites are constrained to locations of interior layered deposits (ILDs), which are relatively young highly eroded surfaces that are typically elevated above the surrounding terrain (Catling et al., 2006; Okubo et al., 2008; Sefton-Nash et al., 2012; Warner et al., 2011) and therefore more susceptible to erosion by oncoming winds due to topographic forcing.

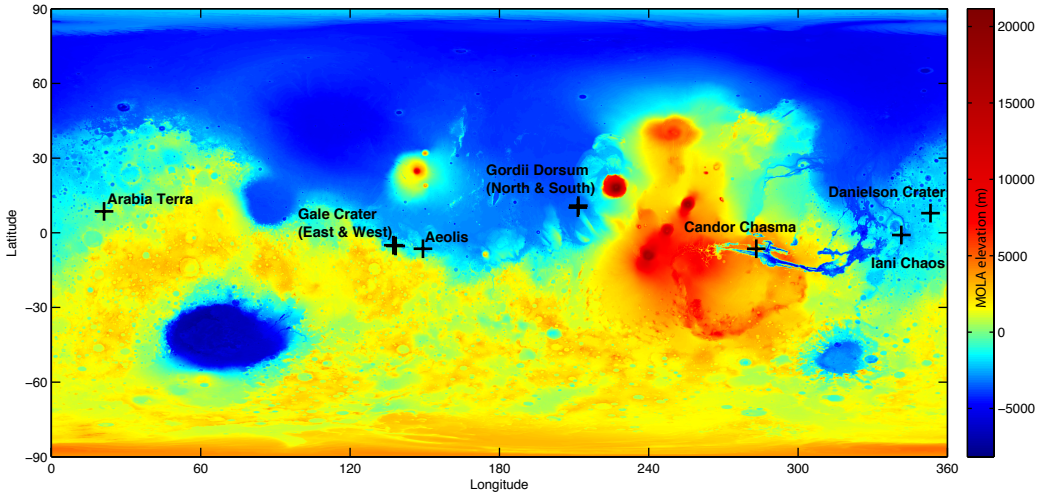

Figure 1: Location of sites selected for this study. Reference map is MOLA 32ppd topography (Zuber et al., 1992).

In order to place upper limits on the age of the least transient wind-eroded features, we also derive model crater retention age fits to established isochrons for young surfaces with populations of small diameter craters (Hartmann, 2005). This study benefits from the use of high resolution (25-60 cm pixel^{-1}) images acquired by the HiRISE instrument on Mars Reconnaissance Orbiter (MRO) (McEwen et al., 2010), which allow fine detail on eroded surfaces and small diameter craters to be resolved.

2. Study sites

2.1. Interior layered deposits

Interior layered deposits (ILDs) are relatively young (Amazonian), easily eroded deposits, characterized by their high albedo, visible layering at a variety of scales and low crater densities (Catling et al., 2006; Okubo, 2010; Ansan et al., 2011; Flahaut et al., 2010; Fueten et al., 2010; Sefton-Nash et al., 2012). Regardless of their formative mechanism, their most recent history has been dominated by aeolian modification (e.g. Figure 3B). ILDs have been identified in chaotic terrain, crater bulges and inter-crater terrain (Malin and Edgett, 2000), but are generally confined to the martian tropics and subtropics. Because ILDs formed relatively late in Mars' history they

are elevated above surrounding terrain which, combined with their generally friable nature, likely makes their surfaces accurate recorders of recent wind directions.

2.2. Identifiable aeolian features I: dunes

Aeolian bedform type is largely determined by the wind regime and the availability of mobile material. Martian dunes (Figure 3E,F) are mostly transverse and crescentic (barchans), as opposed to rare linear longitudinal dunes (Breed et al., 1979; Lee and Thomas, 1995), indicating a predominantly unidirectional wind regime (McKee, 1979). Where more complex wind regimes exist, the gross bedform-normal transport (GBNT) hypothesis proposes that dunes will form with a bedform crest orientation such that the total ('gross') sediment transport normal to the crest is maximized, where total refers to transport from both sides of the crest. The use of gross rather than net transport reflects the idea that e.g. an E-W oriented crest will grow higher if equal amounts of sediment accumulates there from the north as from the south, despite the net transport in that case being zero. There is growing evidence that this approach works well on Earth for both aeolian and sub-aqueous bedforms (e.g., Lancaster (1991); Anthonsen et al. (1996); Lancaster et al. (2010); Reffet et al. (2008); Rubin et al. (2008); Wu et al. (2009)), though disagreement has been noted in some situations or regions (e.g., Lancaster (1991); Clarke et al. (2008); Derickson et al. (2008)).

Estimates of aeolian transport rates on Mars are complicated by a lack of ground truth measurements. Due to Mars' thin atmosphere, wind velocities required to initiate saltation are thought to be much higher on Mars than on Earth (Greeley and Iversen, 1985), with measured and modeled surface wind speeds on Mars appearing to rarely exceed the estimated saltation threshold (Moore, 1985; Bridges et al., 2012). However, the occurrence of major dust storms every few years (with the majority of dust injection presumed to occur via saltation of sand-sized particles) suggests a far more active aeolian environment. In addition, while the majority of large martian dunes appear to be relatively stable and inactive, recent analysis of high resolution images shows substantial dune formation and migration in isolated areas (Edgett and Malin, 2000; Bridges et al., 2007, 2012; Silvestro et al., 2013). The apparent shortfall in modeled winds may be due to their having come from GCMs, which run at a few degrees resolution and thus cannot resolve strong, localized wind gusts that have the greatest influence on transport and erosion (Bridges et al., 2012). Hysteresis effects (Kok, 2010) – i.e., the ability to

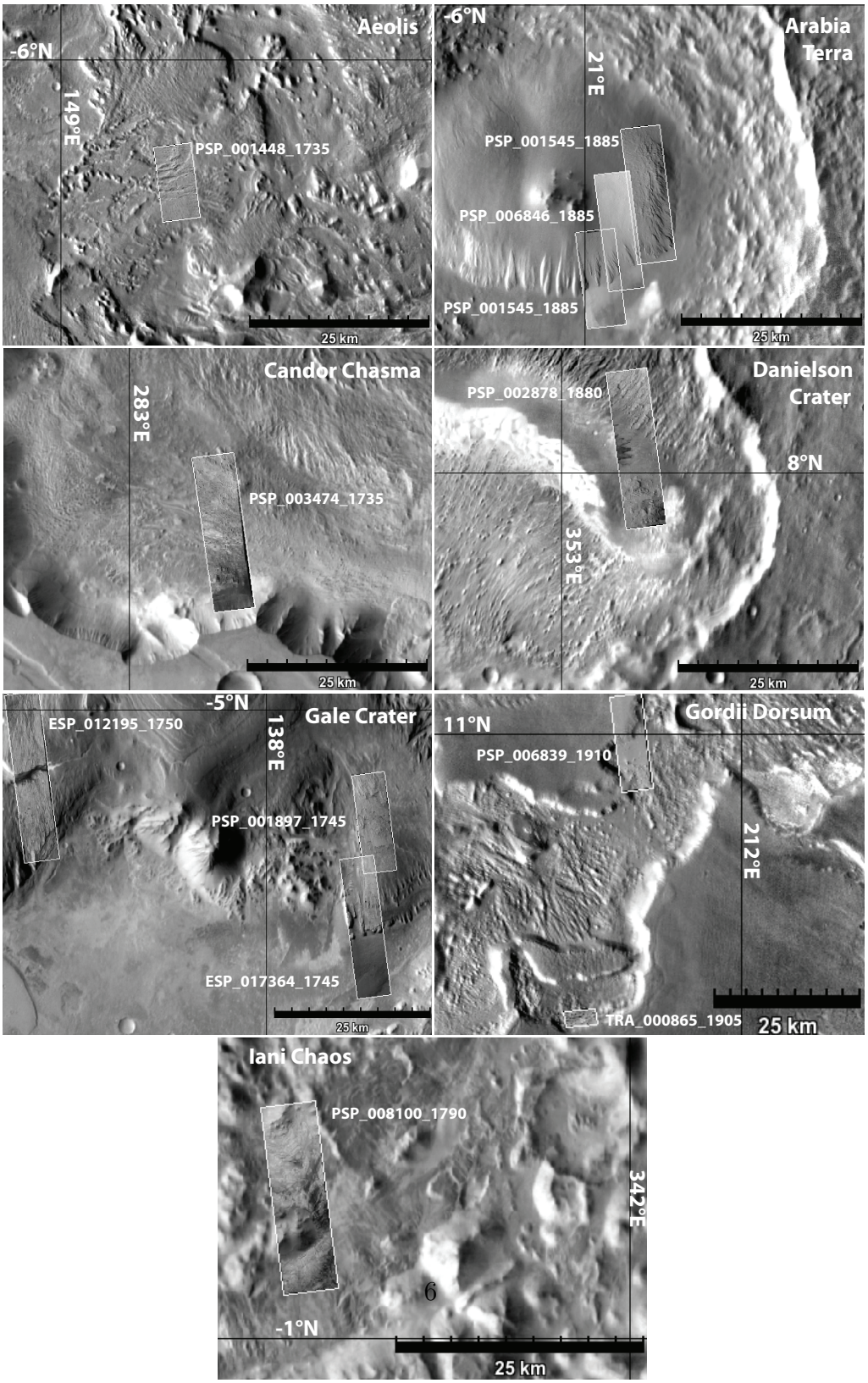

Figure 2: Context of sites selected for this study. Rendered HiRISE stamps indicate our study areas. Background context basemap is from THEMIS daytime IR imagery.

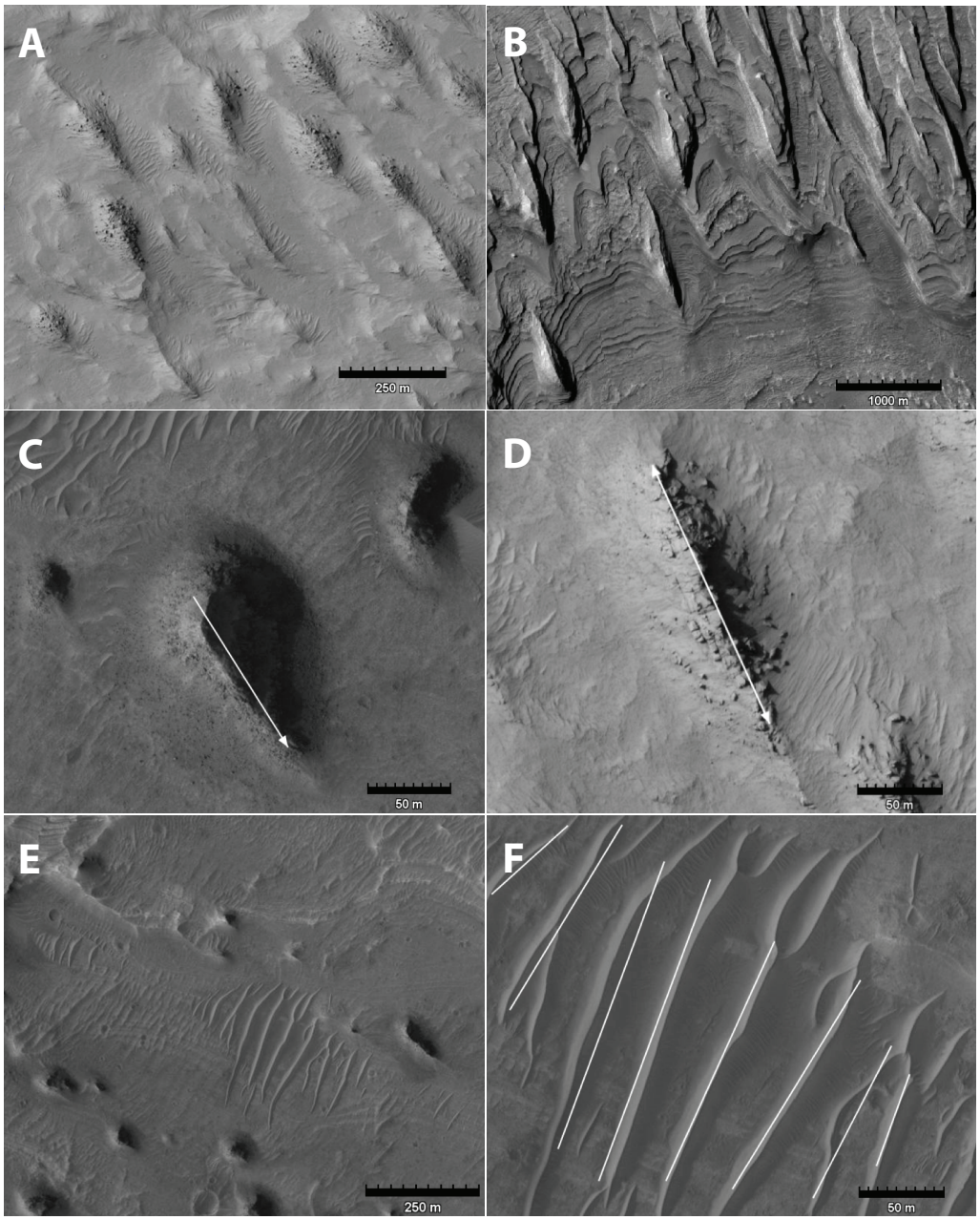

Figure 3: Examples of yardangs and bedforms as seen in HiRISE images listed in Table 2. A) Yardangs in Aeolis. B) Elongate yardangs on layered terrain in east Gale crater C) Teardrop-shaped yardang, allowing dominant wind direction to be inferred. D) Symmetric yardang only allowing inference of wind direction with 180° ambiguity. E) Transverse dune field in Candor Chasma. F) Measurement of dune crest trend, normal to inferred wind trend.

maintain saltation at much lower wind stresses (which must only exceed the impact threshold) once the higher fluid threshold has been exceeded – may also greatly impact these estimates. For active dunes, the length of time taken for a dune to migrate its own length is described as the turnover time (Andreotti et al., 2002), and provides an estimate of the time period over which the dune was formed. Recent modeling of transport properties under Mars surface conditions suggested dune migration rates of a few centimetres per thousand years (Claudin and Andreotti, 2006), in approximate agreement with dune turnover times of 10,000 to 100,000 years estimated by Gardin et al. (2012), which are on the order of timescales of climatic forcing over obliquity cycles. However, observations at Rabe Crater (44 S°) of dune migration of 1–2 cm per Mars year (Fenton, 2006) and dune advancement rates of 0.4–1 m year^{-1} in the tropics (Silvestro et al., 2011, 2013) indicate that more rapid bedform migration occurs in some areas under present day conditions.

This suggests very rapid turnover times of order 50–100 years for a typical 50m wavelength dune. Therefore, dunes may represent wind regimes of about 100 years duration based on observations, although significant uncertainty exists. The martian surface likely holds a combination of slowly migrating (or even 'fossil') dunes that formed during past climate epochs and rapidly migrating dunes that are very active in the present day wind regime.

2.3. Identifiable aeolian features II: yardangs

Yardangs are remnant, wind-eroded, aerodynamic ridges (Figure 3A–D), which form parallel to the wind direction as the result of strong unidirectional wind regimes which cause abrasion and deflation into channels, which are then widened or streamlined (Ward, 1979a). Martian yardangs are larger and more elongate then their terrestrial counterparts (Bridges et al., 2007; de Silva et al., 2010). Yardangs are formed over longer timescales than dunes and are predominantly found on terrains with effectively young model crater retention ages, where erosive resurfacing produces low crater densities, such as ILDs. The surface exposure age gives an upper limit for the yardang formation timescale. Yardang long axis orientation is therefore indicative of recent, but not necessarily modern, wind regimes (Ward, 1979a).

2.4. Surface dating

In order to constrain the maximum age for aeolian features we date ILD surfaces at each site via crater counting using the HiRISE images shown in

Figure 2 and listed in Table 2. We found only six of the ten sites to harbour a sufficient crater population to enable dating: Aeolis, Candor Chasma, Danielson Crater, Gale Crater (east), Gordii Dorsum (south) and Iani Chaos. ILD surfaces within HiRISE image footprints for sites at Arabia Terra, Gale crater (west) and Gordii Dorsum (north) showed fewer than 10 identifiable craters, which we deemed inadequate for reliable crater statistics. Traditionally, error is constrained using the statistical variation between crater populations in separate areas on the same geologic unit (e.g. Warner et al., 2011). However, the small geographic area and young age of ILDs leads to generally low crater counts for this study. For statistical robustness we therefore treat counts for each site as one population. Error bars in Figure 4 represent a factor of two either side of the measured crater density, as suggested by Hartmann (1999). Isochrons represent model crater retention ages based on Hartmann (2005), which represents a refinement and synthesis of crater-dating techniques. Importantly for this study, this includes a correction applied to account for the loss of small (D $\lesssim$ 20 m) bolides in Mars' atmosphere (Popova et al., 2003). Uncertainties are greatest if only small (D $\lesssim$ 100m) craters are used (Hartmann, 2005) and we therefore interpret our crater statistics to give order of magnitude resurfacing age estimates, rather than constrained model ages.

Loss of small craters due to deflation, abrasion and deposition is more likely than for larger craters, which have greater topographic expression. Deviation of our crater statistics from model age isochrons may be an indicator of this process, because the sites we chose by definition must exhibit extensive aeolian modification. Craters $\gtrsim$50 m diameter in Candor Chasma (Figure 4) may represent this aeolian fractionation of the local crater population by erosive capability. However, we do not count large diameter craters in any other regions and this may simply be an artefact of the relatively small size of study areas.

We find most model ages for ILDs to span 0.1-10 Ma. Note that here 'model age' refers to the age since the surface was exposed to the atmosphere, rather than the age of the deposit. However, the absence of larger craters may artificially lower model ages. For comparison, Warner et al. (2011) calculate model ages for a group of ILDs in Iani Chaos, including the deposit we dated, as $24.8^{+3.2}_{-3.3}$ Ma. It is unclear whether the decline in frequency of small diameter craters that we observe at most sites (Figure 4) is due to a larger atmospheric ablation loss than predicted by Popova et al. (2003), preferential aeolian resurfacing of small craters, or an artefact of image resolution, i.e.

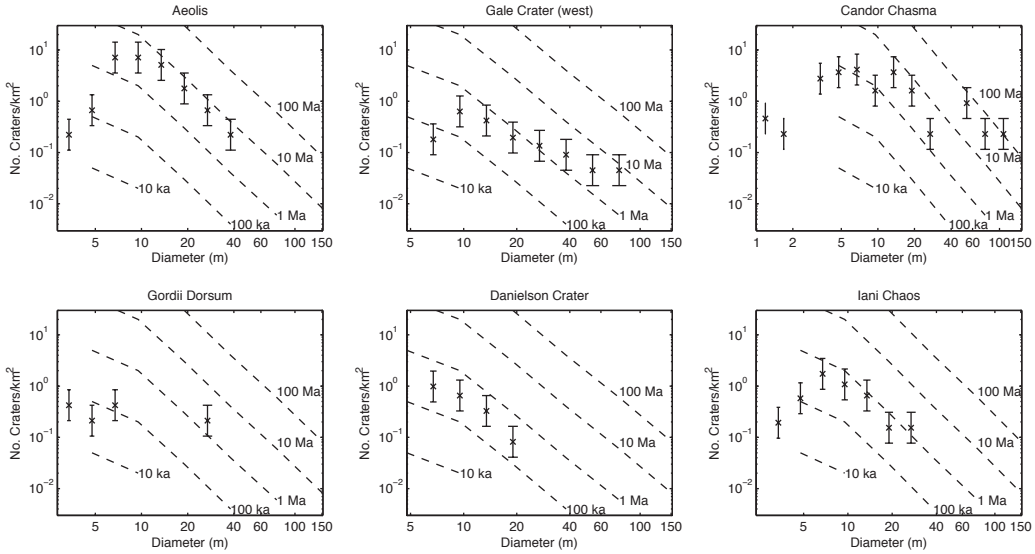

Figure 4: Comparison of crater populations at each of the six sites with isochrons from Hartmann (2005), which applies a correction for ablation of small diameter bolides in Mars' atmosphere. Error bars represent a factor of two, as suggested by Hartmann (1999). See Table 1 for crater counting statistics and age estimates.

Site	No. craters	Area (km^2)	Est. exposure age (Ma)
Aeolis	103	4.5	1–10
Candor Chasma	81	4.3	1–10
Danielson Crater	25	12.2	0.1–10
Gale Crater (East)	117	66.4	0.1–10
Gordii Dorsum (South)	12	9.4	<10
Iani Chaos	118	26.0	0.1–4

Table 1: Crater count statistics and age estimates for each of the six sites with sufficient crater populations. Crater counts at Arabia Terra, Gale Crater (west and south), and Gordii Dorsum (north) are not reported as they showed fewer than 10 countable craters. See Figure 4 for comparison of crater populations with isochrons from Hartmann (2005), which were used to derive the model crater retention ages.

where craters with diameters close to the resolving limit of HiRISE are more difficult to positively identify. In any case, the young model ages suggest aeolian features observed in these deposits will have been formed by recent wind regimes.

3. Method

3.1. Measurement of feature orientation

For our nine sites in seven areas (Figure 1) where heavily wind-eroded ILDs are present, we chose appropriate HiRISE footprints (Figure 2) such that enough area was covered to produce adequate statistics of dune/yardang fields. Details of feature counts, site locations and HiRISE product IDs are shown in Table 2.

Yardang orientation was determined by calculating the azimuth of a vector defined by the two endpoints of their long axis. In some sites yardangs showed a distinctive teardrop shape (e.g. Figures 3C and 5), allowing inference of a unique wind direction. In other sites, yardangs with more elongate and parallel topography allowed only inference of a 180° ambiguous trend line (e.g. Figure 3D).

Dune populations at each site were found only to be transverse, with the exception of Gordii Dorsum (north) and Arabia Terra where no dunes were present within the image footprint (Table 2). Dune orientation was determined by measurement of the trend line parallel to the mean azimuth of each dune crest (Figure 3F). Dune slip-face normals (which, assuming a unimodal wind, approximate wind direction) were perpendicular to this. For transverse dunes wind direction remains 180° ambiguous without detailed inspection of dune morphology, which was beyond the scope of this study.

3.2. Mapping from GCM winds to predicted aeolian feature orientations

A $2^\circ \times 2^\circ$ horizontal resolution run of the MarsWRF GCM (Richardson et al., 2007; Toigo et al., 2012) was sampled at the nine locations listed in Table 2 for each minute of a Mars year, giving a total of 963360 wind vectors at each site, spread uniformly throughout the year. For each point we extracted zonal (u) and meridional (v) wind velocities, the friction velocity, u_*, and the atmospheric density, ρ. u and v were interpolated to an altitude of 1.5m using similarity theory (the lowest model altitude was 10m). Wind speeds at 1.5m were deemed representative of those that control transport via saltation. To account for a range of theories regarding the relationship

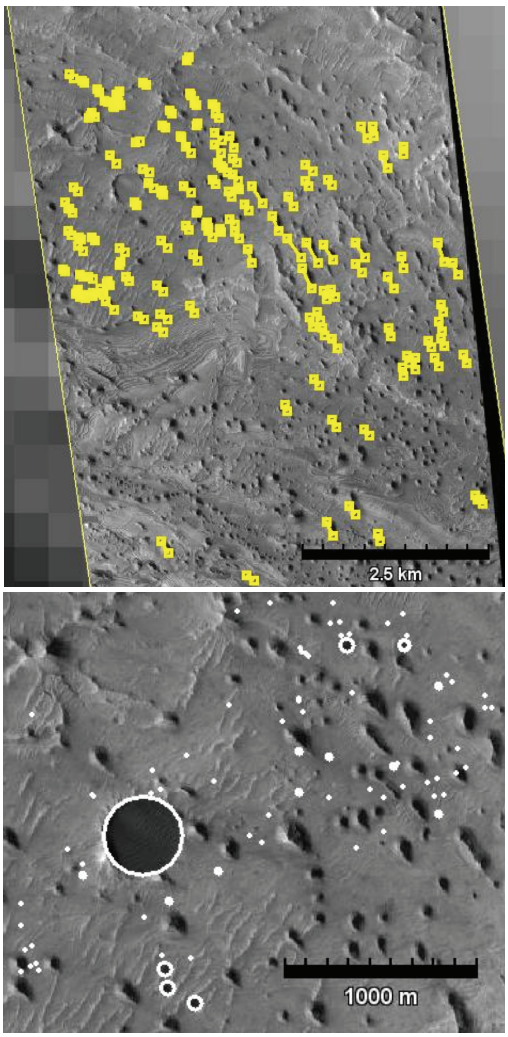

Figure 5: Example measurements of feature orientation (upper) and crater counting (lower) in Candor Chasma.

Site	Lat.	Lon.	HiRISE product	Dunes	Yardangs
Aeolis	-6.40	149.30	PSP_001448_1735	228	65
Arabia Terra	8.61	21.15	PSP_001545_1885 PSP_003655_1885 PSP_006846_1885	0	32
Candor Chasma	-6.40	283.20	PSP_003474_1735	129	131
Danielson Crater	7.90	353.20	PSP_002878_1880	324	44
Gale Crater (East)	-5.30	138.30	PSP_001897_1745	76	93
Gale Crater (West)	-5.00	137.40	ESP_012195_1750 ESP_017364_1745	69	55
Gordii Dorsum (North)	10.90	211.70	PSP_006839_1910	0	96
Gordii Dorsum (South)	10.10	211.50	TRA_000865_1905	125	62
Iani Chaos	-0.90	341.50	PSP_008100_1790	590	72

Table 2: HiRISE image products inspected and number of yardangs and dunes identified at each site.

between wind vectors and the resultant erosion and transport, we derive predicted bedform orientation from GCM output. We use two different numerical mapping approaches specific to dunes and yardangs, both of which require construction of wind stress, σ, given by:

$$\sigma = \rho u_*^2 \tag{1}$$

For a wind with unit direction vector $\hat{\boldsymbol{x}}$, the particle transport flux $\boldsymbol{\tau}$ is defined by:

$$\begin{aligned} \boldsymbol{\tau} &\propto \rho u_*^2 \left(u_* - u_{*t}\right) \hat{\boldsymbol{x}} \qquad \text{if } u_* > u_{*t} \\ \boldsymbol{\tau} &= 0 \qquad\qquad\qquad\qquad\quad \text{otherwise} \end{aligned} \tag{2}$$

where ρ is the air density, u_* is the friction velocity, and u_{*t} is the saltation threshold friction velocity - i.e. the minimum value required to keep grains in saltation. To account for large annual variations in surface pressure on Mars we define a constant saltation threshold stress σ_t and use this to determine u_{*t} via $u_{*t} = \sqrt{\sigma_t/\rho}$.

3.2.1. Approach for dunes

Our approach for dunes is based on the observation that transverse dune crests developed by a temporally dynamic wind field tend not to align normal

or parallel to the direction of sediment transport, but to trend such that the maximum gross bedform-normal transport (GBNT) is achieved (Rubin and Hunter, 1987). We use a modified version of Rubin and Hunter (1987)'s original approach, using the Fryberger flux in Equation (2) to determine the transport and incorporating a saltation threshold as before. As a function of hypothetical dune crest orientation, θ', again defined clockwise from north, our modified GBNT, $T(\theta')$, is given by:

$$T(\theta') = \sum_{i=1}^{n} \rho_i u_{*i}^2 \left(u_{*i} - u_{*t}\right) \left| \frac{u_i \cos\theta' - v_i \sin\theta'}{\sqrt{u_i^2 + v_i^2}} \right| \qquad \forall\ i \text{ where: } u_{*i} > u_{*t} \tag{3}$$

where the first term is the Fryberger transport flux and the second term is the absolute value of the transport flux direction vector projected into the bedform-normal direction. The optimum dune crest orientation θ is then given by maximizing $T(\theta')$. We solve this using a simple grid search in the range $0^\circ \leq \theta' < 180^\circ$ such that T is maximized for each site (Figure 6). To explore sensitivity to saltation threshold, we calculate predicted dune crest line orientations θ for: zero stress threshold $\sigma_t = 0$ Nm^{-2}; a moderate stress threshold $\sigma_t = 0.008$ Nm^{-2} and a higher threshold $\sigma_t = 0.016$ Nm^{-2}. For comparison, 0.008 Nm^{-2} corresponds to $u_{*t} \approx 0.7$ ms^{-1} for an average martian surface air density.

For sites where the GBNT function showed significant secondary maxima (observed only at Iani Chaos), we also show the expected dune crest orientation for wind stress thresholds of $\sigma_t = 0.008$ Nm^{-2} and $\sigma_t = 0.016$ Nm^{-2} for the secondary GBNT peak.

3.2.2. Approach for Yardangs

We count MarsWRF surface wind vectors unweighted, weighted by wind stress and weighted by particle transport flux in angular bins to illustrate the distribution of transport in annual wind fields that may contribute to yardang formation (Figure 7). We determine the the directions of primary and secondary maxima in these distributions to indicate the most likely yardang-forming weathering direction (Figure 9). In addition to weighting by Fryberger flux, we also investigate the impact of assuming that rock abrasion rates, which are responsible for producing yardangs, vary as u_*^5 rather than as u_*^3. In that case particle transport flux $\boldsymbol{\tau}$ has the relationship:

$$\boldsymbol{\tau} \propto \rho u_*^4 \left(u_* - u_{*t}\right) \hat{\boldsymbol{x}} \tag{4}$$

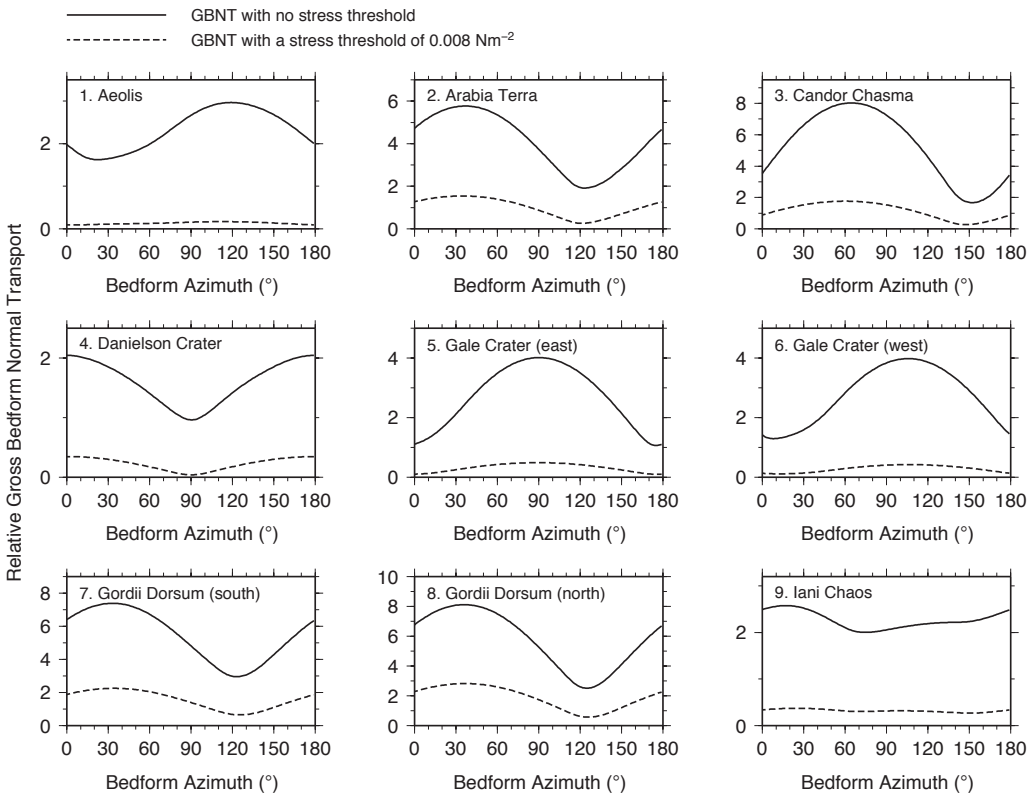

Figure 6: Gross bedform-normal transport (Rubin and Hunter, 1987) calculated by solving equation 3 over the 180° angular range of possible bedform trend line orientations.

This was suggested by the results of Anderson (1986), and can be thought of conceptually as the transported particle flux varying as u_*^3, with the erosion produced by particles impacting the rock face varying as u_*^2 (related to the kinetic energy of the particles). We refer to particle transport flux calculated in this manner as 'yardang flux'.

4. Results

The orientations of transverse dune trend lines and yardang long axes were measured at each site (e.g. Figure 5). Azimuth distributions for each feature are plotted on Rose diagrams normalized to percentage of the total population for that feature (Figures 8 and 9). The mean direction of yardangs (blue) and dunes (red) should be approximately normal to each other if both populations were formed under the same unidirectional wind regime.

4.1. MarsWRF GCM output

To illustrate annual wind fields (Figure 7) we count MarsWRF surface wind vectors in 64 angular bins and plot the normalized frequency of vectors 1) unweighted 2) weighted by the vector mean stress 3) weighted by flux defined by Fryberger (1979) (Equation 2) 4) weighted by Fryberger flux with a stress threshold $\sigma_t = 0.008$ Nm^{-2} 5) weighted by Fryberger flux with $\sigma_t = 0.016$ Nm^{-2}, and 6) weighted by 'yardang flux', where $\boldsymbol{\tau} \propto \rho u_*^4 (u_* - u_{*t})$ and $\sigma_t = 0.008$ Nm^{-2}.

4.2. Dunes

Transverse dune crest orientations at each site are plotted as trend lines with 180° symmetry (Figure 8). In Figure 8 we show the predicted orientations of bedform trend lines calculated by the numerical formulations involving maximizing GBNT (Equation 3) for various wind stress thresholds. We also show the orientation of a significant secondary GBNT maximum observed at Iani Chaos only. If MarsWRF wind vectors represent the present dune-forming wind field and our chosen dune fields are active, then the predicted trend lines (red lines in Figure 8) should agree with the mean transverse dune crest trends observed.

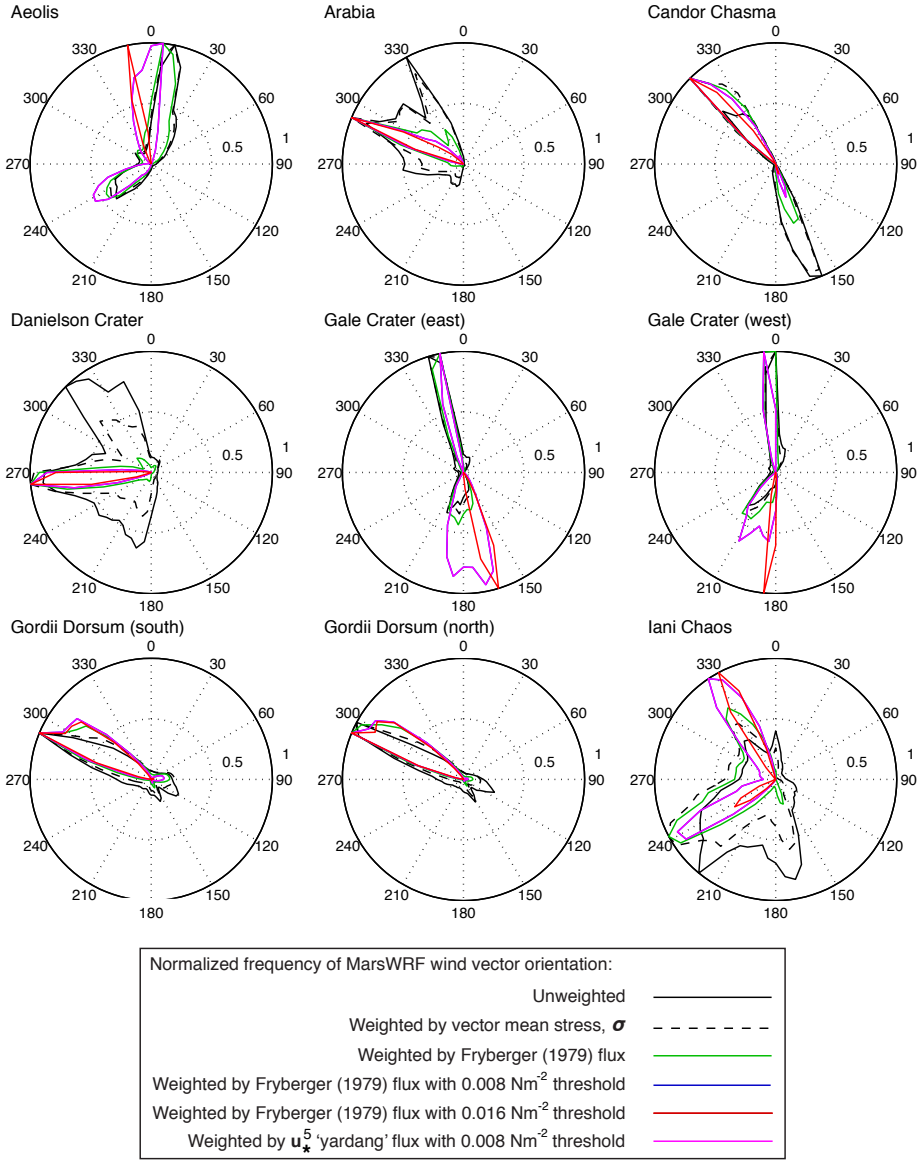

Figure 7: Azimuth distribution of surface wind vectors produced by the MarsWRF GCM over one Mars year in the present climate regime. Lines are drawn between frequency counts in each of 64 bins of angular width 5.625°. Black solid lines are vector frequency in each bin. Dashed lines are weighted by wind stress, σ, which takes into account atmospheric density (Equation 1). Green, blue and red lines represent wind vectors weighted by the wind stress formulation of Fryberger (1979) (Equation 2) with threshold stresses of 0, 0.008 and 0.016 Nm^{-2}, respectively. Magenta lines represent vectors weighted by yardang flux (Equation 4) with a threshold of 0.008 Nm^{-2} (to investigate yardang erosion dependancies presented by Anderson (1986)).

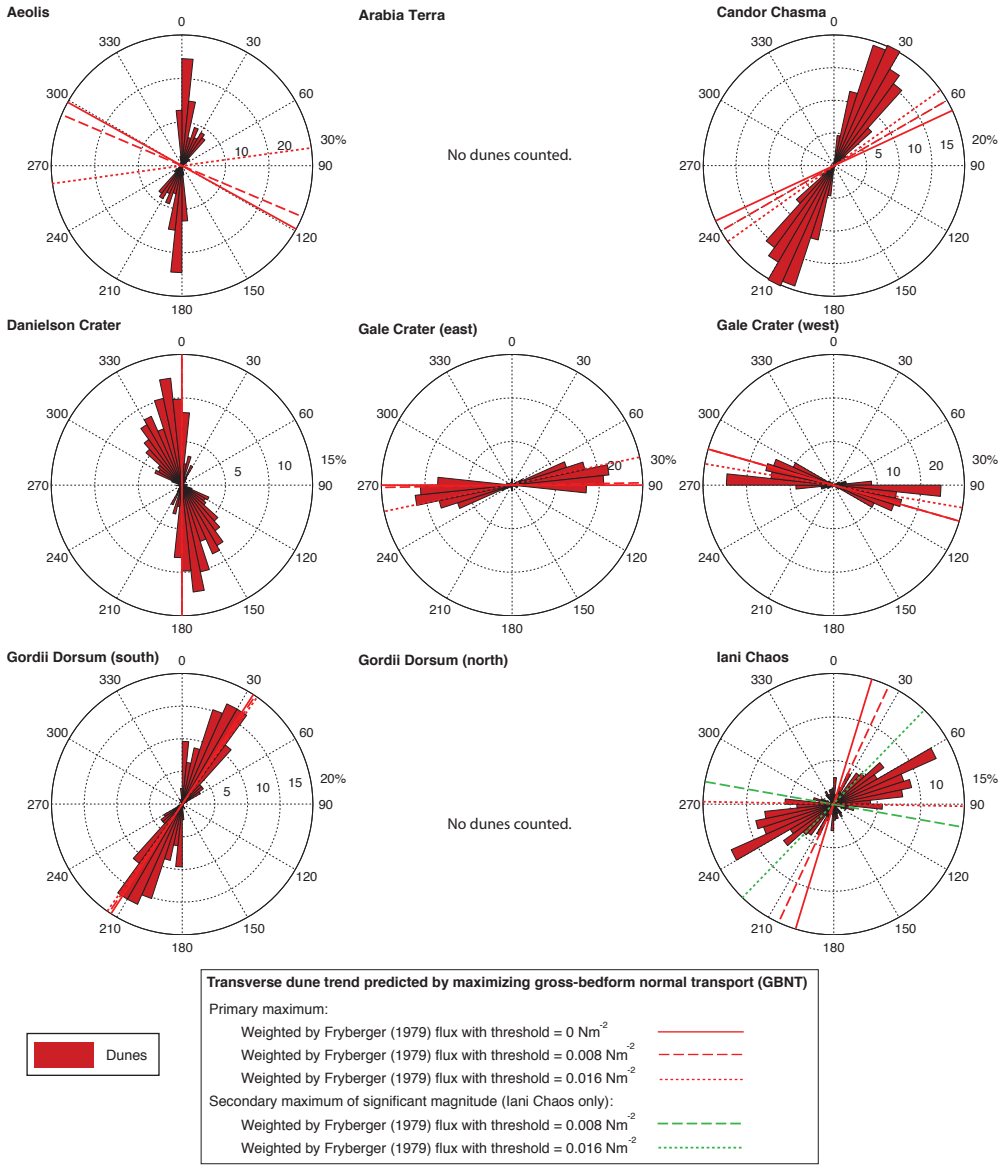

Figure 8: Rose diagrams of trend lines representative of average dune crest orientation. Angular bins are 6° and bar radii are sized according to percentage of the total population of each feature. Also shown are the results from two different methods for prediction of transverse dune crest trends by maximizing GBNT calculated from the MarsWRF GCM's annual vector wind field (Equation 3). For Iani Chaos, a secondary but significant local maxima in GBNT is also plotted (see Figure 6).

4.3. Yardangs

For yardangs, unambiguously inferred transport directions (in the case of tear drop shaped features) were retained when plotting directions (Figure 9). 180° ambiguous yardangs were rare and typically numbered less than ∼10%, but where they occured yardang direction was plotted in the same sense as neighbouring unambiguous yardangs, which were assumed to be exposed to similar wind fields. For Danielson crater, sufficient ambiguity was present for all yardangs that we plot them as 180° ambiguous trends.

The most likely yardang-forming weathering directions are plotted on Figure 9 as the directions of principle and secondary maxima in weighted vector frequencies in Figure 7. Secondary orientations in dashed circles indicate vector frequency maxima that are present for low-order weightings, but that become subdued for higher order weightings of u_*^3 and u_*^5 (yardang flux). Winds in these directions with lower erosive power may therefore be less likely to contribute to yardang formation.

If modeled wind fields are of the same orientation as those that formed measured yardang populations, then principle wind stress directions (numbers in Figure 9) should match yardang long axis orientations. However yardang formation in multi-directional wind field is currently not well understood, even on Earth, and further investigation into the relationship between non-unidirectional wind fields and yardang orientation is warranted.

5. Discussion

5.1. Dunes and GBNT

Good matches are seen between dunes and maximum GBNT at 4 of 7 sites: Danielson Crater, Gale Crater (east and west) and Gordii Dorsum south. Use of higher stress thresholds ($\sigma_t = 0.016$ Nm^{-2}) typically improves matches where wind regimes are multi-directional. Sites where GBNT is least impacted by choice of threshold tend to show predominantly uni-directional wind regimes with respect to Fryberger flux (i.e., Danielson Crater and both sites in Gordii Dorsum).

At Candor Chasma dune orientations are within 15-30° of predicted and the match improves for progressively higher stress thresholds. At Iani Chaos the best match is seen for the highest threshold 0.016Nm^{-2}. However, Iani Chaos shows a low amplitude in GBNT over the total angular range (Figure 6), implying a distribution of wind vectors from many directions over the course of the year, which is reflected in the angular dispersion of high vector

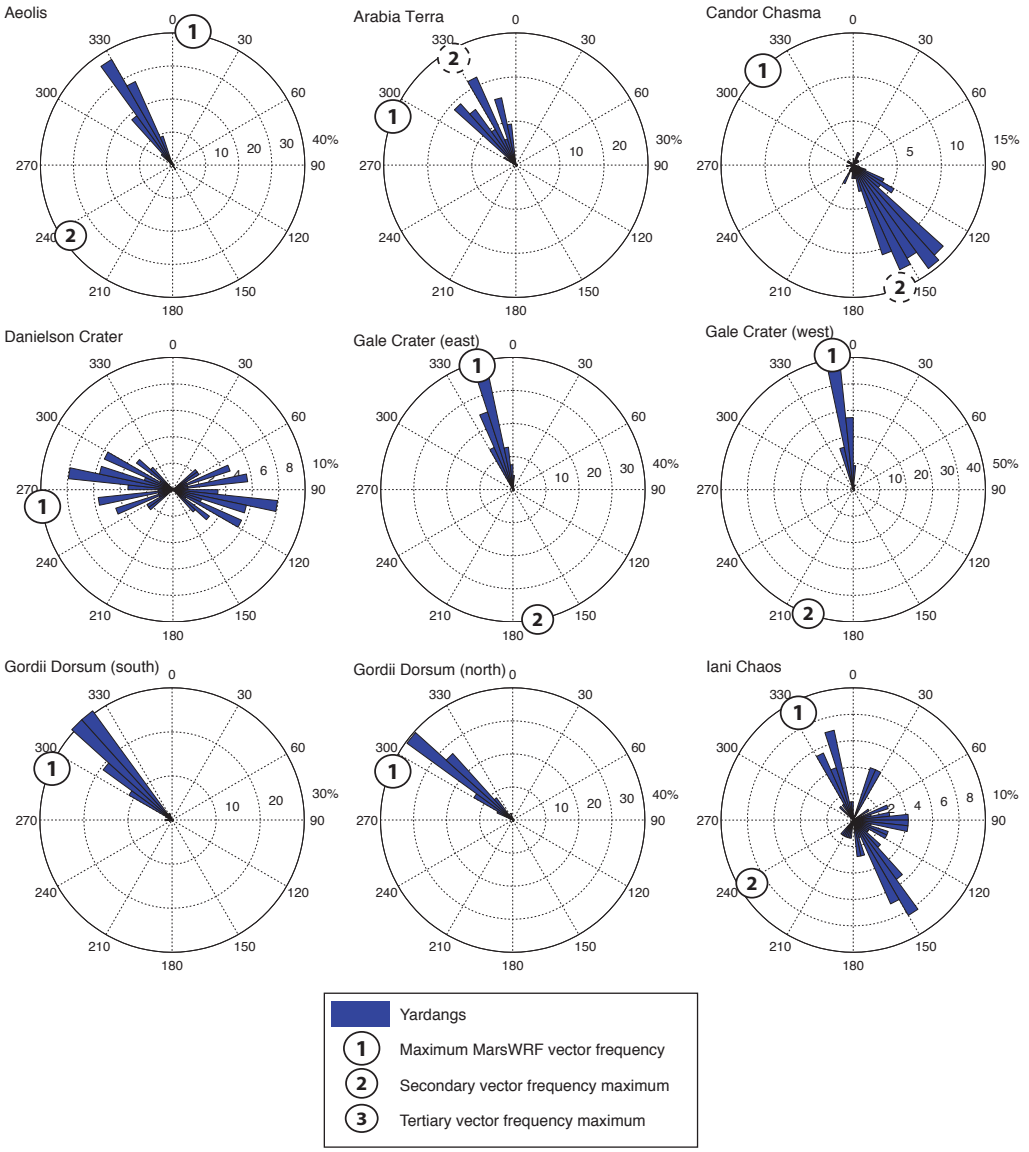

Figure 9: Rose diagrams showing the orientation of yardang long axes (blue). Angular bins are 6° and bar radii are sized according to percentage of the total population of each feature. Also shown are the primary and secondary (where present) wind vector frequency maxima, derived from MarsWRF GCM's annual vector wind field shown in Figure 7. Secondary orientations in dashed circles indicate directions prominent when low-order u_* weightings were applied.

frequencies in Figure 7. Consequently, the direction of the second highest GBNT inflexion for Iani Chaos in Figure 8 (green lines) also shows moderate agreement with observed dune populations.

Aeolis shows the worst match between modeled and observed dune orientations, with the maximum GBNT at all thresholds more nearly perpendicular to, than aligned with, the observed dune orientations. We discuss plausible reasons for this mismatch in Section 5.3.

5.2. Yardangs

There is good agreement for most regions between yardang long axis orientation and primary or secondary wind stress maxima, with the exception of Aeolis (Figure 9). Arabia Terra yardangs are dispersed over about a 50° range, but match well with the secondary maximum, defined by low-order weighted and non-weighted peak in wind vector frequency. The direction of the primary transport flux maximum is offset from the edge of the yardang population by about ∼15°. Candor Chasma also shows a good match to the secondary direction ('2' in dashed circle, Figure 9), which shows up as a maxima only if no wind stress weightings are included (i.e., though winds are predicted to occur often in this direction, their associated fluxes are predicted to be far weaker than those in the direction labeled '1'). Danielson Crater could be regarded as a good fit if yardang sense were able to be constrained to a unique 180° angular range. Excellent matches are seen between predicted and observed yardang orientations at both sites in Gale Crater. Both Gordii Dorsum south and north sites show similar offsets of ∼10-20° between GCM dominant wind directions and yardangs, but dunes at the south site show a better match to GBNT predictions from the GCM. Therefore Gordii Dorsum presents a reasonable case for further investigation into consistent offsets between dunes and yardangs, which may yield information on wind field change if present dune fields are active and if higher spatial resolution wind models produce similar predicted orientations. Yardangs poorly match GCM predicted orientations, as well as dunes, at the Aeolis site. Local terrain is somewhat variable (Figure 2), perhaps implying that higher-resolution modeling is required to resolve dune- and yardang-forming winds (also see discussion of Aeolis in Section 5.3). In Iani Chaos the primary GCM-wind stress orientation matches one of the several yardang populations, but both GCM vectors and yardang orientations are spread over a wide angular range (Figure 9). In sites where multiple yardang populations occur, such as Iani Chaos, they are clustered into separate regions of homogeneous orientation.

If unidirectional wind fields are required for yardang formation (which is not clear from terrestrial or planetary studies, though seems plausible given the nature of their formation), then yardangs could be formed in localized areas of unidirectional winds that are beyond the spatial resolution of the GCM. In modeled wind fields that show more than one dominant direction (e.g. Iani Chaos, Figure 7) then one or more directions could be selectively halted or diverted by local topography in sub-regions, leaving some surfaces exposed to an effectively unidirectional erosion regime. This effect may explain observations of multiple yardang populations in close proximity that are oriented differently. However, this discussion would be aided by a firmer answer to whether yardangs can form in bidirectional winds or whether the very existence of yardangs implies unidirectional winds. For some locations, weighting of modeled wind vectors by u_*^5, instead of u_*^3, tends to produce a unidirectional 'spike' in the primary direction, but a greater angular dispersion for secondary directions (Figure 7). In these cases (Gale Crater east and west) yardangs are aligned with only the sharp primary direction, supporting the theory that yardang formation tends to occur only in effectively unidirectional wind fields.

5.3. Overall match of dunes and yardangs to GCM predictions

Poor matches between maximum GBNT and dune orientation at Aeolis may be due to the choice of metric (GBNT, Fryberger (1979) flux and threshold choice). However, the GCM spatial resolution of 2° is far lower than the dunes themselves and hence may not represent the dune-forming winds, especially in regions of complex topography where sub-grid cell topographic diversion is not resolved. Use of a higher spatial resolution model may better resolve localized dune-forming winds. If neither of these factors could be verified as responsible for the mismatch i.e. the present GCM does resolve dune-forming (and yardang-forming) winds and our choice of metric is an accurate bulk representation of the dune-forming process, then it would be possible to more confidently ascribe the offset as due to disequilibrium of both feature populations with the present day wind regime, implying a more ancient origin for dunes and yardangs under a different wind field. In any case, this site presents an opportunity for further study to investigate the impact of higher resolution GCMs.

We found no dunes at the Arabia Terra or Gordii Dorsum (north) locations, but yardangs at Arabia Terra deviate approximately $\sim$30° from the

peak vector frequency of GCM winds, while those at Gordii Dorsum (south) show a better match with a deviation of $\sim 10^{\circ}$.

At Gale Crater (east and west) both dunes and yardangs show excellent agreement between predicted and observed orientations, perhaps a surprising result given the variable local topography. Though at 2° lateral resolution the GCM does not resolve the detailed crater circulations that one might expect to strongly influence these dune fields. While the excellent match shown here suggests that the crater circulations might be dominated by regional flows, this may also be coincidental and a focus of future work will be using mesoscale ($\sim$1.5-4km resolution) modeling to assess the impact on predictions of resolving any crater flows.

Observation of active ripples in NW Gale Crater (Silvestro et al., 2013) supports a modern age for dunes in Gale but does not necessarily imply the same for dunes in this study because their ripple locations do not coincide with our study areas. Proof that dunes in our Gale study areas are in equilibrium with the present-day wind field could be sought through 1) observation of present-day dune activity and 2) agreement of mesoscale models with our GCM results.

Dunes at Danielson crater show excellent agreement with maximised GBNT, while yardangs agree less well, but still match within $\sim 15^{\circ}$. While yardang-forming winds predicted from GCM output are predominantly unidirectional, those that are unweighted and weighted by vector mean wind stress show a wide angular range and several significant maxima (Figure 7). This could contribute to the uncertainty in determining unique yardang sense at this location, i.e. minor yardang erosion in a non-principle direction may have weathered direction specific-features.

Close matches at Candor Chasma are seen between predicted orientations and dunes (within $\sim 25^{\circ}$) and yardangs (within $\sim 10^{\circ}$ of the secondary maximum marked '2'). Gordii Dorsum (south) shows similarly good matches with a slightly greater offset for yardangs. The significance of this offset remains to be tested, but could imply that yardangs are less in equilibrium with present dune-forming wind regimes that are well represented by GCM output, or that the yardang-forming wind regime is not well captured by our interpretation of GCM output.

While there is tentative agreement between the orientations of dunes and some yardangs at Iani Chaos (Figures 8 and 9), there are additional yardang populations that may be representative of very localized unidirectional wind regimes unresolved by the GCM, or alternately by past wind fields. In either

case, complex local topography warrants the use of a mesoscale GCM to resolve the variation in wind fields and therefore feature orientation over short distances.

6. Conclusions

We studied nine sites that are expected to be representative of modern day wind fields on Mars and measured the orientations of features with short (dunes) and long (yardangs) timescales of formation.

We selected interior layered deposits because they are young and easily wind-eroded. Model crater retention ages derived for ILDs via comparison of crater size frequency distributions to those defined by (Hartmann, 2005) were found to be on the order of 0.1-10 Ma, in moderate agreement with previous estimates (available for Iani Chaos only (Warner et al., 2011)), and confirming ILDs applicability to modern wind field determination. Remaining uncertainties in isochron development are reflected by factor of 2 error bars on model ages. For sites where yardangs and dune orientations disagree, model ages represent an upper limit on yardang age and therefore timescales for changes in the local wind field.

Transverse dunes were counted at 7 of 9 sites, while yardang orientations were analysed at all sites. Feature orientations were compared to output from the MarsWRF GCM running at a spatial resolution of 2°. Dune orientations agreed very well with predictions made by maximising gross bedform-normal transport (Rubin and Hunter, 1987) and weighting by flux as defined by Fryberger (1979). Better agreements were generally observed when wind stress thresholds were applied, with the maximum applied threshold $\sigma_t = 0.016$ Nm^{-2} giving the best match for several sites. Application of wind stress thresholds had the greatest effect on predicted dune orientation for sites with multi-directional wind fields. Sites with annually invariant, unidirectional wind fields showed no change with threshold. Poor agreement was seen for sites with extreme local topography such as chasma and chaos regions, implying that local topographic effects are important and therefore higher resolution mesoscale models are required before further model comparison can be made.

Yardang orientations agree well in most cases with a primary or secondary transport-weighted maxima in annual wind vector frequencies. Close inspection of maxima in weighted annual wind vector frequencies thus appears to provide a basis for meaningful prediction of yardang orientations

in multidirectional wind fields in future studies. The agreement of multiple different yardang populations in close proximity with multiple maxima in an annual wind field may indicate local scale topographic blocking of some dominant wind directions and/or focusing of one, thus producing the highly unidirectional wind regime that appears required for yardangs to form.

The number of regions with good agreement between measured and predicted feature orientations by the MarsWRF GCM increases our confidence in using this model to predict winds elsewhere on Mars. Broadly, aeolian features on ILDs provide an excellent way to measure present day wind directions and validate GCMs, however, care must be taken in areas of high topographic relief and higher resolution models are required to make more complete comparison. We find that comparison of yardang long axes to directional maxima in modeled wind vector frequencies, and comparison of dune orientation to maximum GBNT are appropriate treatments.

Finally, we demonstrate that comparison of past and present wind fields inferred from aeolian feature orientations to those predicted by GCMs may be both a viable technique for model validation and for gaining insight into recent climate variations on Mars.

7. Acknowledgements

Elliot Sefton-Nash and Nick Teanby are grateful for funding form the Leverhulme Trust for this work. Nick Teanby was also funded by the the UK Science and Technologies Facilities Council (STFC). Claire Newman was funded by NASA MFRP grant number NNX11AF59G, and all GCM simulations were performed on the High End Computing facility at NASA Ames.

References

Anderson, R. S., 1986. Erosion profiles due to particles entrained by wind: Application of an eolian sediment-transport model. Geological Sopciety of America Bulletin 97 (10), 1270–1278.

Andreotti, B., Claudin, P., Douady, S., 2002. Selection of dune shapes and velocities Part 1: Dynamics of sand, wind and barchans. Eur. Phys. J. B 28, 321–339.

Ansan, V., Loizeau, D., Mangold, N., Moulic, S. L., Carter, J., Poulet, F., Dromart, G., Lucas, A., Bibring, J.-P., Gendrin, A., Gondet, B., Langevin,

Y., Masson, P., Murchie, S., Mustard, J., Neukum, G., 2011. Stratigraphy, mineralogy, and origin of layered deposits inside Terby crater, Mars. Icarus 211 (1), 273–304.

Anthonsen, K. L., Clemmensen, L. B., Jensen, J. H., 1996. Evolution of a dune from crescentic to parabolic form in response to short-term climatic changes: Rabjerg Mile, Skagen Odde, Denmark. Geomorphology 17, 63–77.

Bagnold, R. A., 1941. The Physics of Blown Sand and Desert Dunes. Methuen, New York.

Bitter, J. G. A., 1963a. A study of erosion phenomena: Part 1. Wear 6, 5–21.

Bitter, J. G. A., 1963b. A study of erosion phenomena: Part 2. Wear 6, 169–190.

Breed, C. S., Grolier, M. J., McCauley, J. F., 1979. Morphology and distribution of common 'sand' dunes on Mars: Comparison with the Earth. J. Geophys. Res. Solid Earth 84 (B14), 8183–8204.

Bridges, N. T., Bourke, M. C., Geissler, P. E., Banks, M. E., Colon, C., Diniega, S., Golombek, M. P., Hansen, C. J., Mattson, S., McEwen, A. S., Mellon, M. T., Stantzos, N., Thomson, B. J., 2012. Planet-wide sand motion on Mars. Geology 40, 31–34.

Bridges, N. T., Geissler, P. E., McEwen, A. S., Thomson, B. J., Chuang, F. C., Herkenhoff, K. E., Keszthelyi, L. P., Martínez-Alonso, S., 2007. Windy Mars: A dynamic planet as seen by the HiRISE camera. Geophysical Research Letters 34 (23), 1–7.

Catling, D. C., Wood, S. E., Leovy, C., Montgomery, D. R., Greenberg, H. M., Glein, C. R., Moore, J. M., Mar 2006. Light-toned layered deposits in Juventae Chasma, Mars. Icarus 181 (1), 26–51.

Clarke, L. B., Werner, B. T., Okihiro, M., 2008. Surf zone megaripple orientation: Measurements and models. J. Geophys. Res. 113 (C03018).

Claudin, P., Andreotti, B., 2006. A scaling law for aeolian dunes on Mars, Venus, Earth, and for subaqueous ripples. Earth Planet. Sci. Lett. 252, 30–44.

591 de Silva, S. L., Bailey, J. E., Mandt, K. E., Viramonte, J. M., 2010. Yardangs
592 in terrestrial ignimbrites: Synergistic remote and field observations on
593 Earth with applications to Mars. Planet. Space Sci. 58, 459–471.

594 Derickson, D., Kocurek, G., Ewing, R. C., Bristow, C., 2008. Origin of a
595 complex and spatially diverse dune-field pattern, Algodones, southeastern
596 California. Geomorphology 99, 186–204.

597 Edgett, K. S., Malin, M. C., 2000. New views of Mars eolian activity, materi-
598 als, and surface properties: Three vignettes from the Mars Global Surveyor
599 Mars Orbiter Camera. J. Geophys. Res. Plan. 105 (E1), 1623–1650.

600 Fenton, L. K., 2006. Dune migration and slip face advancement in the Rabe
601 Crater dune field, Mars. Geophys. Res. Lett. 33 (20).

602 Fenton, L. K., Richardson, M. I., 2001. Martian surface winds: Insensitivity
603 to orbital changes and implications for aeolian processes. J. Geophys. Res.
604 106 (E12), 32,885–32,902.

605 Flahaut, J., Quantin, C., Allemand, P., Thomas, P., 2010. Morphology and
606 geology of the ILD in Capri/Eos Chasma (Mars) from visible and infrared
607 data. Icarus 207 (1), 175–185.

608 Fryberger, S. G., 1979. Dune forms and wind regime. In: McKee, E. D. (Ed.),
609 U.S. Geological Survey Profile Pap. 1052, Washington, pp. 137–169.

610 Fueten, F., Racher, H., Stesky, R., MacKinnon, P., Hauber, E., McGuire,
611 P., Zegers, T., Gwinner, K., 2010. Structural analysis of interior layered
612 deposits in Northern Coprates Chasma, Mars. Earth Planet. Sci. Lett. 294,
613 343–356.

614 Gardin, E., Allemand, P., Quantin, C., Silvestro, S., Delacourt, C., 2012.
615 Dune fields on Mars: Recorders of a climate change? Planet. Space Sci.
616 60 (1), 314 – 321.

617 Greeley, R., Iversen, J. D., 1985. Wind as a gelogical process on Earth, Mars,
618 Venus and Titan. Cambridge University Press.

619 Greeley, R., Leach, R. N., Williams, S. H., White, B. R., Pollack, J. B.,
620 Krinsley, D. H., Marshall, J. R., 1982. Rate of wind abrasion on Mars. J.
621 Geophys. Res. 87 (12), 9–24.

Greeley, R., Skypeck, A., Pollack, J. B., 1993. Martian aeolian features and deposits: Comparisons with general circulation model results. J. Geophys. Res. 98 (E2), 3183–3196.

Haberle, R. M., Pollack, J. B., Barnes, J. R., Zurek, R. W., Leovy, C. B., Murphy, J. R., Lee, H., Schaeffer, J., 1993. Mars atmospheric dynamics as simulated by the NASA Ames General Circulation Model: 1. The zonal-mean circulation. J. Geophys. Res. Plan. 98 (E2), 3093–3123.

Hartmann, W. K., 1999. Martian cratering VI: Crater count isochrons and evidence for recent volcanism from Mars Global Surveyor. Met. Plan. Sci. 34, 167–177.

Hartmann, W. K., 2005. Martian cratering 8: Isochron refinement and the chronology of Mars. Icarus 174, 294–320.

Kok, J., 2010. An improved parameterization of wind-blown sand flux on Mars that includes the effect of hysteresis. Geophys. Res. Lett. 37 (L12202), 1–6.

Lancaster, N., 1991. The orientation of dunes with respect to sand-transporting winds: a test of Rubin and Hunter's gross bedform-normal rule. Acta Mechanica Supplement 2, 89–102.

Lancaster, N., Nickling, W. G., Gillies, J. A., 2010. Sand transport by wind on complex surfaces: field studies in the McMurdo Dry Valleys, Antarctica. J. Geophys. Res. (Earth Surface) 115 (F03027).

Lee, P., Thomas, P. C., 1995. Longitudinal dunes on Mars: Relation to current wind regimes. J. Geophys. Res. Plan. 100 (E3), 5381–5395.

Malin, M. C., Edgett, K. S., 2000. Sedimentary Rocks of Early Mars. Science 290, 1927–1937.

McEwen, A. S., Banks, M. E., Baugh, N., Becker, K., Boyd, A., Bergstrom, J. W., Beyer, R. A., Bortolini, E., Bridges, N. T., Byrne, S., Castalia, B., Chuang, F. C., Crumpler, L. S., Daubar, I., Davatzes, A. K., Deardorff, D. G., DeJong, A., Delamere, W. A., Dobrea, E. N., Dundas, C. M., Eliason, E. M., Espinoza, Y., Fennema, A., Fishbaugh, K. E., Forrester, T., Geissler, P. E., Grant, J. A., Griffes, J. L., Grotzinger, J. P., Gulick, V. C., Hansen, C. J., Herkenhoff, K. E., Heyd, R., Jaeger, W. L., Jones,

654 D., Kanefsky, B., Keszthelyi, L., King, R., Kirk, R. L., Kolb, K. J., Lasco,
655 J., Lefort, A., Leis, R., Lewis, K. W., Martinez-Alonso, S., Mattson, S.,
656 McArthur, G., Mellon, M. T., Metz, J. M., Milazzo, M. P., Milliken, R. E.,
657 Motazedian, T., Okubo, C. H., Ortiz, A., Philippoff, A. J., Plassmann, J.,
658 Polit, A., Russell, P. S., Schaller, C., Searls, M. L., Spriggs, T., Squyres,
659 S. W., Tarr, S., Thomas, N., Thomson, B. J., Tornabene, L. L., Houten,
660 C. V., Verba, C., Weitz, C. M., Wray, J. J., 2010. The High Resolution
661 Imaging Science Experiment (HiRISE) during MRO's Primary Science
662 Phase (PSP). Icarus 205 (1), 2–37.

663 McKee, E. D., 1979. A study of global sand seas. Professional paper 1052,
664 United States Geological Survey.

665 Merrison, J., Bechtold, H., Gunnlaugsson, H., Jensen, A., Kinch, K., Norn-
666 berg, P., Rasmussen, K., 2008. An environmental simulation wind tunnel
667 for studying Aeolian transport on mars. Planet. Space Sci. 56, 426–437.

668 Moore, H. J., 1985. The Martian Dust Storm of Sol 1742. J. Geophys. Res.
669 Plan. 90 (S01), 163–174.

670 Newman, C. E., Lewis, S. R., Read, P. L., 2005. The atmospheric circulation
671 and dust activity in different orbital epochs on Mars. Icarus 174 (1), 135–
672 160.

673 Okubo, C. H., 2010. Structural geology of Amazonian-aged layered sedimen-
674 tary deposits in southwest Candor Chasma, Mars. Icarus 207, 210–225.

675 Okubo, C. H., Lewis, K. W., McEwen, A. S., Kirk, R. L., 2008. Relative
676 age of interior layered deposits in southwest Candor Chasma based on
677 high-reolsution structural mapping. J. Geophys. Res. 112 (E12002).

678 Popova, O., Nemtchinov, I., Hartmann, W. K., 2003. Bolides in the present
679 and past martian atmosphere and effects on cratering processes. Met. Plan.
680 Sci. 38 (6), 905–925.

681 Reffet, E., Courrech du Pont, S., Hersen, P., Douady, S., Fulchignoni, M.,
682 2008. Longitudinal dunes on Titan: A laboratory approach. In: Planetary
683 Dunes Workshop: A Record of Climate Change, held April 29-May 2, 2008
684 in Alamogordo, New Mexico. LPI Contribution No. 1403, p.58-59.

685 Richardson, M. I., Toigo, A. D., Newman, C. E., 2007. PlanetWRF: A general
686 purpose, local to global numerical model for planetary atmospheric and
687 climate dynamics. Journal of Geophysical Research: Planets 112 (E9).

688 Rubin, D. M., Hunter, R. E., 1987. Bedform alignment in directionally vary-
689 ing flows. Science 237, 276–278.

690 Rubin, D. M., Tsoar, H., Blumberg, D., 2008. A second look at western Sinai
691 seif dunes and their lateral migration. Geomorphology 93, 335–342.

692 Sefton-Nash, E., Catling, D. C., Wood, S. E., Grindrod, P. M., Teanby, N. A.,
693 2012. Topographic, spectral and thermal inertia analysis of interior layered
694 deposits in Iani Chaos, Mars. Icarus 221, 20–42.

695 Silvestro, S., Vaz, D., Ewing, R., Rossi, A., Fenton, L., Michaels, T., Flahaut,
696 J., Geissler, P., 2013. Pervasive aeolian activity along rover Curiosity's
697 traverse in Gale Crater, Mars. Geology 41, 483–486.

698 Silvestro, S., Vaz, D. A., Fenton, L. K., Geissler, P. E., 2011. Active aeo-
699 lian processes on Mars: A regional study in Arabia and Meridiani Terrae.
700 Geophys. Res. Lett. 38 (20), 1–6.

701 Toigo, A. D., Lee, C., Newman, C. E., Richardson, M. I., 2012. The impact
702 of resolution on the dynamics of the martian global atmosphere: Varying
703 resolution studies with the MarsWRF GCM. Icarus 221 (1), 276–288.

704 Ward, A. W., 1979a. Yardangs on Mars: Evidence of Recent Wind Erosion.
705 J. Geophys. Res. 84 (B14), 8147–8166.

706 Ward, W. R., 1979b. Present obliquity oscillations of Mars: Fourth-order
707 accuracy in orbital e and I. J. Geophys. Res. Solid Earth 84 (B1), 237–
708 241.

709 Warner, N. H., Gupta, S., Kim, J.-R., Muller, J.-P., Le Corre, L., Morley, J.,
710 Lin, S.-Y., McGonigle, C., 2011. Constraints on the origin and evolution
711 of Iani Chaos, Mars. J. Geophys. Res. Plan. 116 (E06003), 1–29.

712 Wu, J., Wang, Y., Cheng, H., 2009. Bedforms and bed material transport
713 pathways in the Changjiang (Yangtze) Estuary. Geomorphology 104 (3-4),
714 175–184.

715 Zuber, M. T., Smith, D. E., Solomon, S. C., Muhleman, D. O., Head, J. W.,
716 Garvin, J. B., Abshire, J. B., Bufton, J. L., 1992. The Mars Observer Laser
717 Altimeter Investigation. J. Geophys. Res. 97 (E5), 7781–7797.